Alireza Setayeshgar
Department of Mechanical Engineering,
University of Alberta,
Edmonton, AB T6G 2G8, Canada
e-mail: Setayesh@ualberta.ca

Michael G. Lipsett
Department of Mechanical Engineering,
University of Alberta,
Edmonton, AB T6G 2G8, Canada
e-mail: mlipsett@ualberta.ca

Charles R. Koch
Department of Mechanical Engineering,
University of Alberta,
Edmonton, AB T6G 2G8, Canada
e-mail: Bob.koch@ualberta.ca

David S. Nobes[1]
Department of Mechanical Engineering,
University of Alberta,
Edmonton, AB T6G 2G8, Canada
e-mail: dnobes@ualberta.ca

Particle Motion in a Macroscale, Multiwavelength Acoustic Field

Particle motion due to ultrasonic acoustic radiation in a macroscale, multiwavelength acoustic chamber is investigated and compared with available theories. Primary acoustic radiation force theory has been extensively developed to predict single particle motion in a microscale, single-node acoustic chamber/channel. There is a need to investigate the applicability of this theory to macroscale, multiwavelength acoustic channels utilizing the acoustic radiation force for separating polydispersed particles. A particle-tracking velocimetry (PTV) approach for measuring individual particle motion is developed specifically to track particles as they densify at an acoustic pressure node. Particle motion is tracked over the lifetime of their motion to a node. Good agreement between the experimental and theoretical results is observed in the early stages of particle motion, where particles can be considered individually. Only in the densified region of the acoustic pressure node is there some mismatch with theory. The acoustic energy density of the acoustic chamber, a parameter intrinsically associated with the system by the theory, is also determined experimentally for different conditions and shown to be constant for all investigated system settings. The investigation demonstrates the capability of available theory in predicting the motion of polydispersed particles in macroscale, multiwavelength acoustic chambers. [DOI: 10.1115/1.4027777]

Introduction

The need to separate or sort fine particles from liquids has led to the use of the ultrasonic acoustic radiation force in microscale flow systems, including the areas of biotechnology [1–3] and drug delivery [4–6]. Ultrasonic acoustic pressure has been used to concentrate mammalian cells in cell culture fermentations where efficiencies up to 99% are achieved in removing cells from the stream without cell damage [1]. Separation of blood cells suspended in a microchannel is also continuously performed using this approach [2] with maximum efficiency of 99.975%, which is comparable with other more traditional methods, such as centrifugation. Here, the advantage is in that the separation is applied to only a very small sample volume. The method is also applicable and being used in medical applications, such as drug delivery [4–6]. In Ref. [4], it is shown that the efficiency of targeted imaging with microbubble-base agents can be improved by using ultrasonic acoustic radiation force, and localized drug delivery can also be improved [5].

In all of these applications, the sizes of the flow channels are of a similar order of the wavelength of the acoustic field. Also, particles are well dispersed and can be considered to act independently of each other. Under these conditions, the force applied by a standing acoustic field can be well described by the currently available single particle/acoustic field interaction theory [7]. The theory finds the primary acoustic force on a single particle in an inviscid fluid. There are various approaches based on this theory for estimating primary acoustic force in the literature for different conditions, such as the primary acoustic force on a single particle suspended in viscous fluid [8] or the primary acoustic force on a compressible particle [9]. These theories allow the design and development of processes and technology at the microscale. At this scale, the piezoelectric transducers are designed to have a single-wavelength [10], half-wavelength [11], or quarter-wavelength [12] resonance within the width of the microchannel. While the acoustic pressure force and consequently the separation efficiency increases by having these setups, the piezoelectric transducers become more complex and there is a limit to the maximum system volume flow rate.

Although this technology has been developed well at the microscale, it has not however been utilized to address larger scale problems, such as particle separation in macroscale channels with relatively large volume flow rates. There are several applications, such as the treatment of water [13,14] and food processing [15], in which ultrasonic acoustic separation technology have been implemented through removal of its volume flow rate limitations by using batch operation. There are a limited number of works on utilizing ultrasonic acoustic pressure at the macroscale in a continuous system, such as Ref. [16], in which micron-sized beads are separated from water in a 25.4×25.4 mm (1×1 in.) cross section flow channel.

The aim of this research is to study the applicability of using an ultrasonic acoustic radiation force for particle separation in macroscale flows where polydispersed distribution particles are suspended in the containing fluid. In these systems, the scale of the flow field is many times that of the wavelength of the acoustic field and can be termed a multiwavelength system. As the larger particles separate to pressure nodes (or antinodes), it can be expected that the properties of the acoustic field (i.e., coherence and dampening) will be affected. Smaller particles, which are traveling to the closest pressure nodes (or antinodes) at a slower rate due to their smaller size, are affected consequently by the formation of densification bands by larger particles. The densified particles at the pressure nodes can potentially increase the acoustic dampening effect, resulting in lower primary acoustic force on the particles. Dampening of the pressure acoustic wave and scattering of the pressure acoustic wave off the walls and densified particles bands can also be expected in the multiwavelength acoustic chambers/channels [17]. These effects, which are difficult to theoretically predict [18], need to be experimentally investigated.

Imaging methods have been used to investigate and characterize the acoustic radiation force and the separation process by different investigators [19–22]. The movement and aggregation of a suspension of yeast cells under the influence of a standing ultrasonic field has been investigated [19]. During the aggregation process, the velocity of cells was measured using particle image

[1]Corresponding author.

Contributed by the Fluids Engineering Division of ASME for publication in the JOURNAL OF FLUIDS ENGINEERING. Manuscript received January 7, 2014; final manuscript received April 28, 2014; published online September 10, 2014. Assoc. Editor: Alfredo Soldati.

velocimetry (PIV) and compared with current theories [7] that describe cell and particle motion. In Ref. [20], the primary and secondary acoustic radiation forces on single monodispersed particles are measured. The acoustic energy density is also determined by tracking individual particles affected by ultrasonic acoustic pressure. Acoustophoresis in a 377 μm microchannel is also studied [21] by imaging and tracking polystyrene particles affected by an acoustic radiation force in the channel. The monodisperse particles were tracked individually, and the resultant velocity measurements were compared with a single particle theory governing the primary acoustic force. The primary acoustic radiation force on single particles is also investigated using μPIV [22] and the results compared with available theories and results in Ref. [21]. In all of these cases, the particles are homogenously mixed field before the acoustic field is applied. PIV, which requires an optimum seeding density, can only be applied in a limited fashion during the initial stages of the application of the acoustic field. No information is collected on the phenomenon once the particles are too segregated to PIV to be applied consistently.

The validity of the current particle/acoustic field interaction theory, which only describes the forces generated on a single particle in a homogeneous acoustic field, needs to be tested in large-scale, multiwavelength systems. This would allow the theory to be used for design of particle separation systems using an acoustic field at the macroscale. Determining particle motion and hence the forces applied using imaging techniques has many advantages. However, the complexity of the acoustic separation process in macroscale acoustic chambers limits the ideal conditions needed for accurate PIV measurements. The time-dependent process at the macroscale taking place on a real polydispersed size distribution of particles changes their distribution homogeneity dramatically. Information on the homogeneity of the acoustic field in a multinode acoustic system to determine the impact of system scale on the modeling approach is also lacking.

A method is needed that allows for the tracking of particles through a complete cycle of the separation process as the acoustic field becomes more inhomogeneous. The data collected can then be used to compare with the predictions of ultrasonic acoustic pressure single-particle theory [23] over the complete field. The data collected can also be used to characterize the macroscale acoustic chamber used to develop the standing acoustic field by studying the acoustic energy density for different cases. A custom approach based on PTV has been developed to investigate these systems [24]. The main issue in using a classic PTV method is the gradual change in the distribution of particles. Here, the source of particle motion is the acoustic pressure force, which depends on the position of particle relative to the acoustic field rather than the force on the PIV seeding particles due to the fluid flow. This paper investigates the validation of single particles theory for a macroscale, multiwavelength acoustic chamber using the developed PTV method. The experimental setup for generating the phenomenon is discussed, and the velocity field results for three different particle/acoustic field cases are compared with single particles theory; the acoustic chamber is also characterized.

Primary Acoustic Force Theory. The acoustic radiation effect was first identified in Ref. [25] while observing suspended cork dust in water. The cork dust was trapped in a resonated acoustic tube, originally to measure the speed of sound in 1874. The phenomenon was studied by investigating the primary acoustic radiation force on particles for different conditions [7]. By introducing a velocity potential for an inviscid fluid containing an incompressible sphere smaller than the wavelength of the standing acoustic wave, the time-averaged acoustic radiation force on the sphere was derived. Later, the work was continued and developed in Ref. [9], where the primary radiation force on a compressible sphere particle in a fluid was calculated. The time average force on a particle was also derived as the gradient of a potential function defined as the summation of the kinetic and potential energy of the acoustic wave at the location of the particle [23].

Assuming that particles are suspended in an ideal fluid, the particles are compressible and their diameters are small compared to the wavelength of the acoustic field; the force on a single spherical particle is defined as the gradient of the acoustic potential energy [23]. For a standing-wave acoustic field where the radiation force is much larger than a progressive wave, fluid pressure and velocity can be expressed as functions of spatial location and time using

$$p(x,y,z,t) = p_a(y,z)\sin(\kappa x)\sin(\omega t) \tag{1}$$

$$v(x,y,z,t) = v_a(y,z)\cos(\kappa x)\cos(\omega t)\boldsymbol{k} \tag{2}$$

where p_a and $v_a = (p_a/\rho_f c)$ are the fluid pressure and velocity amplitude of the wave as a function of spatial location (x,y,z) and time (t) with y the coordinate in the direction of gravity, c the fluid sound speed, ρ_f the density of the surrounding fluid, $\kappa = (2\pi/\lambda)$ the wave number of the wave, $\omega = 2\pi f$ the angular frequency, f the frequency of the acoustic source, and $\boldsymbol{k}$ the unit vector in the x direction.

The time-averaged ultrasonic primary acoustic force [26] on a single particle suspended in an inviscid fluid is

$$F_{ac} = 3V_0 E_{ac}\kappa\eta\sin(2\kappa x) \tag{3}$$

where V_0 is the particle volume and E_{ac} is the acoustic energy density, which is a measure of the effect of acoustic chamber through the effect of generated acoustic pressure p_a in the field and is defined as

$$E_{ac} = \frac{p_a^2\beta_f}{4} \tag{4}$$

where β_f is the fluid compressibility and is inversely proportional to speed of sound in a material. The acoustic contrast factor (ACF), η, is a function of the density ratio $(\tilde{\rho})$ and compressibility ratio $(\tilde{\beta})$ of the particle to fluid. This factor is defined as

$$\eta = \frac{1}{3}\left[\frac{5\tilde{\rho}-2}{2\tilde{\rho}+1} - \tilde{\beta}\right] \tag{5}$$

where particle-to-fluid density ratio $(\tilde{\rho})$ and particle-to-fluid compressibility ratio $(\tilde{\beta})$ are defined as

$$\tilde{\rho} = \frac{\rho_p}{\rho_f} \tag{6}$$

$$\tilde{\beta} = \frac{\beta_p}{\beta_f} \tag{7}$$

where indices p and f refer to particle and fluid, respectively.

The ACF (η) plays an important role in the primary acoustic radiation force and is a function of two different properties of the system. The influence of this parameter can be investigated by comparing the effect of particle acoustic properties (density and speed of sound) for cases in which particles are suspended in water. The acoustic specifications of different example materials are listed in Table 1. These materials are also indicated in Fig. 1. In this figure, the variation of ACF for a material of constant

Table 1 Acoustic specifications of different sample materials

Material	Density (g/cm^3)	Speed of Sound (m/s)	ACF (η)
Glass	2.5	5600	0.57
Silicone oil	0.76	1350	−0.26
Polystyrene	1.1	2350	0.23

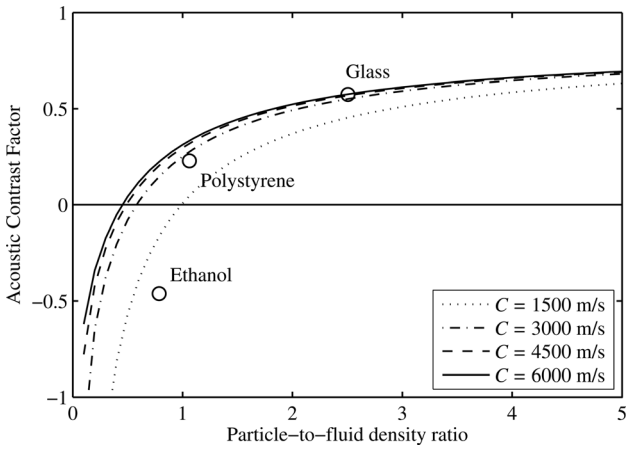

Fig. 1 Achieved ACF for constant speed of sound values; indicated ACF for different materials in water. *c* is speed of sound in particle.

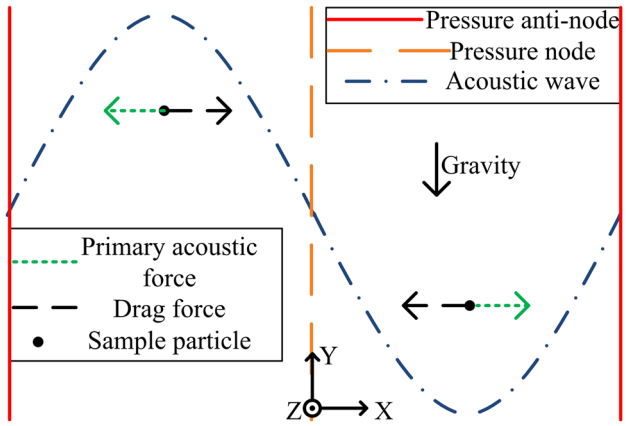

Fig. 2 Pressure node and antinode locations and transverse (horizontal) forces directions on particles; longitudinal acoustic wave is shown in the transverse direction

speed of sound values but different densities is plotted. According to these curves, the density ratio has more influence on ACF for lower values of particle density where the ACF value is negative. A negative value of ACF indicates that the particle will be attracted to a pressure antinode, whereas a particle with a positive ACF value, such as a glass particle in water, will be forced toward a pressure node. As the particle-to-fluid density ratio increases for a constant speed of sound particle-to-fluid ratio, the ACF approaches an asymptote. It is also notable that the constant speed of sound curves for $c = 3000\,\text{m/s}$ to $c = 6000\,\text{m/s}$ are approximately coincident. This indicates that the influence of speed of sound on the ACF reduces for higher values and the force on the particle in water is mostly governed by its density.

Considering the forces acting on a single particle in the x direction (horizontal), as shown in Fig. 2, the particle velocity due to the primary acoustic pressure force can be determined by accounting only for the resistance drag body force on the particle. Gravity and buoyancy forces are applied in the x direction (vertical) and do not affect the transverse motion of the particle. The motion of a particle with a positive ACF traveling toward the nearest pressure node is assumed to be due to the primary acoustic force overcoming the drag force. The main assumption is that the inertia of the single particle is due to its relatively low velocity and consequently low Reynolds number of flow. This assumption is applicable for micron-sized particles [26].

Considering a Stokes drag force applied on the particle while influenced by an acoustic pressure force, the balance of forces on the single particle is

$$3V_0E_{ac}\kappa\eta\sin(2\kappa x) = 6\pi\mu aV \tag{8}$$

in which μ is the viscosity of containing fluid, a is the particle radius, and V is particle velocity. By rearranging this equation, the velocity of a single particle affected by acoustic radiation pressure in the wave propagation direction can be found as

$$V = \frac{V_0E_{ac}\kappa\eta}{2\pi\mu a}\sin(2\kappa x) \tag{9}$$

This highlights that the maximum velocity of the particle is proportional to the energy density of the acoustic field. The acoustic energy density is a function of the piezoelectric transducer used to generate the acoustic field and its properties, the acoustic chamber properties, and, more specifically, how energy is coupled between them. Generally this parameter, which is constant for a particular acoustic cell, is estimated from experimental data by studying the motion of different types of particles in various conditions for the acoustic field [18].

Experimental Setup and Procedure

A schematic of the general experimental setup used is shown in Fig. 3(*a*) and compared to a digital image of the actual setup used in Fig. 3(*b*). The acoustic field is generated in a static fluid (degassed distilled water) contained within the acoustic cell. A high power piezo-electric transducer forms one side of the chamber and is excited with a continuous sine wave. The wave is generated via a function generator and power amplifier. In Fig. 3(*a*), an imaging configuration with a thin light sheet of a laser illuminating the region of interest is schematically depicted. A combination of a high-speed camera and a lens on a region of interest in the acoustic cell are used to image the motion of particles.

Acoustic Chamber. The acoustic chamber is a $30 \times 25 \times 65$ mm^3 glass cell with a 1.5 MHz resonance frequency, high-power, piezoelectric transducer forming one side of the chamber (Sonosep Technologies Inc. [27]). This transducer has a narrow bandwidth over which maximum energy can be transferred into the acoustic field. The cell is aligned vertically, and the transverse/horizontal acoustic pressure wave influences the particles in the transverse direction. The piezoelectric transducer is excited by applying a harmonically sinusoidal voltage generated from a function generator (Tektronix AFG320 GPIB V3) at 1.52 MHz. The signal is amplified (70 mV–22 V) by a high-power amplifier (ENI240L).

The experiments are carried out for three different particle sets. The individual particle properties are given in Table 2. The coefficient of variation (CV) of particle size (diameter) distribution is the ratio of standard distribution of the probability density function of size of particles to the mean value of their size and is used to determine the distribution of the acoustic force on particles based on Eq. (9). The speed of sound for hollow glass particles (particle set 2 (PS-2) and particle set 3 (PS-3)) is assumed to be the same as speed of sound for solid glass particles. This assumption is made due to the low variation of the acoustic contrast factor for those fluid/particle sets with respect to speed of sound for glass as shown in Fig. 1. The system is first tested on particle set 1 (PS-1), which has a low CV of particle size distribution to validate the single-particle theory [23] for the setup. PS-2 and PS-3—which have a larger CV, that is, wider size distribution—are the main focus of the investigation. The volume concentration of particles in water for all of the experiments is set to 0.05%.

Imaging System. The imaging system consists of a continuous wave laser and a two-dimensional piezo-scanning mirror combined to illuminate the area of interest. A high-speed camera with a long-working-distance lens is used to capture images of the particle fields. The laser (Laserglow Technologies, LRS-0532-PF)

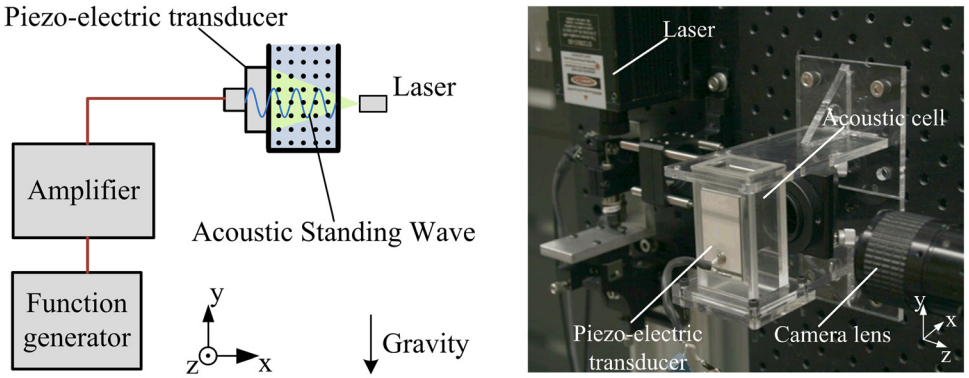

(*a*) (*b*)

Fig. 3 (*a*) Schematic of the main experimental components and (*b*) digital image of the experimental setup

Table 2 Properties of particle sets used in experiments

Particle Set	Description	Mean Diameter (μm)	CV	Density (g/cm^3)	Speed of Sound (m/s)	ACF (η)
PS-1	Silica microspheres (cospheric)	8	10%	1.8	6400	0.49
PS-2	Hollow microspheres (potters 60P18)	18	35%	0.6	6400	0.14
PS-3	Hollow microspheres (potters 110P18)	10	45%	1.1	6400	0.35

operates in a continuous mode with wavelength of 532 nm and is capable of providing power of up to 2 W. The laser beam is swept using one mirror of the two-dimensional scanner, which consists of two rotating mirrors driven using two piezoelectrics. The swept laser beam is passed through a collimation lens located at the focal distance of the mirrors to generate a parallel laser sheet. The beam is reflected toward the region of interest using the second control mirror, which helps in correcting the alignment of the laser plane due to possible misalignment of the illumination components. A high-speed camera (DRS Technologies, Lightning® RDTPlus) attached to a 65 mm f/2.8 lens (Canon Inc., MP-E 65 mm) with a working distance range of 40–100 mm and that is capable of magnification factor of up to five is used for imaging. The camera is capable of collecting images at 500 fps at full frame (1280 × 1024) and maximum of 16,000 fps at reduced resolution. It has a 10-bit CMOS sensor and is equipped with a transistor-transistor logic trigger.

Experimental Procedures. A consistent experimental procedure is followed for all the presented results. Degassed distilled water is used to avoid the generation of cavitation bubbles in regions of low pressure at antinodes of the acoustic field in the cell. Particle volume concentration is set to 0.05% by suspending an initially measured mass of particles in a known volume. After assuring the mixture is in a homogeneous state in terms of particle concentration, the experiment starts with triggering of the camera to collect frames at the set speed. Other components are triggered in time with camera acquisition in a specific order following the commencement of the experiment. The function generator that drives the piezoelectric transducer is triggered after 100 ms to define the exact time for the onset of acoustic excitement. The piezoelectric transducer excitation voltage was set to 22 V. The particles start their transverse motion to the nearest pressure nodes following the activation of the piezoelectric transducer. The camera is operated at 1000 fps with the resolution of 512 × 512 pixels, and the lens magnification is set to three, leading to a depth of field of 88 μm and working distance of 50 mm. The piezoelectric transducer receives the voltage input for 1 s, which is enough to displace all particles to a pressure node in the field. The transverse velocity of particles is obtained by postprocessing the camera images.

Image Postprocessing. In developing an appropriate strategy for postprocessing and determining particle motion and velocity, some basic understanding of the phenomenon in needed. The main characteristic of this phenomenon is the time dependency, which changes particle distribution within the imaged region of interest. To highlight this, example raw images are shown in Fig. 4 of particle fields before and after the acoustic field is applied that show how the acoustic field concentrates particles into vertical bands. In Fig. 4(*a*), a homogeneous particle distribution is shown. In-focus particles detected with a particle identification algorithm are circled. In Fig. 4(*b*), the acoustic field, which has planes of nodal pressure oriented vertically, has been applied and the particles have migrated to pressure nodes in the acoustic field. Again, particles detected with the particle identification algorithm are circled. Both figures highlight a significant problem for determining the velocity and hence the force acting on the particles. For the homogeneous case before the acoustic field is applied, particle detection is relatively easy, with the individual particles being clearly defined. As the particles concentrate under the applied acoustic field, the interparticle distance reduces and particle images begin to overlap. Individual particle detection therefore becomes more difficult with increasing particle concentration that occurs with time.

As seen in Fig. 4(*b*), the acoustic field has multiple nodes within the field. The spacing is a function of the acoustic properties of the system and the driving frequency of the piezoelectric transducer. This can be compared with microscale acoustic chambers, which can have a half-wavelength [28] or quarter-wavelength [12] system and only one node. Despite having a limitation in volume flow rate, microscale chambers provide a stronger and more homogenous acoustic field. However, the current macroscale chamber produces multinodes where the field distribution is not as homogenous, making particle identification difficult and hence determination of particle motion and velocity.

PTV Analysis. The particles are tracked for 1 s, over which densification occurs, of which Fig. 4(*b*) is an example. Custom

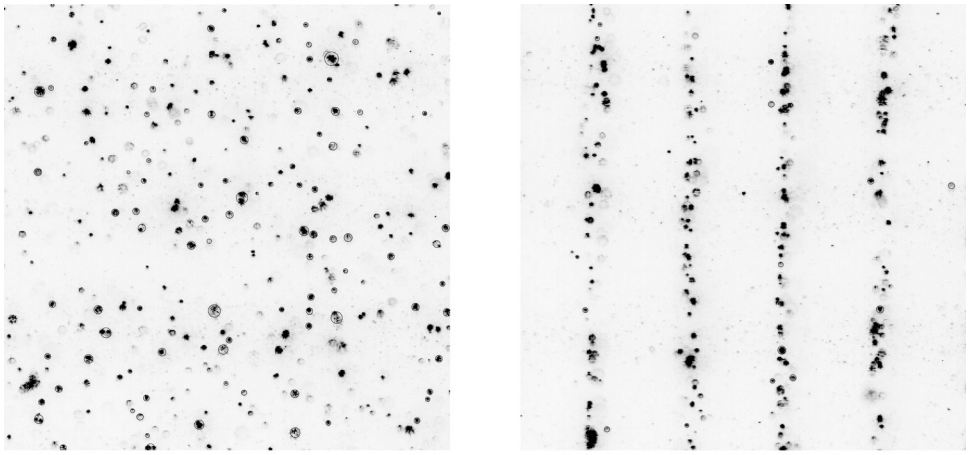

(*a*) (*b*)

Fig. 4 Detection of particles in images in different situations: (*a*) even distribution of particles before applying the acoustic wave and (*b*) densification of particles to bands due to the acoustic radiation force

code (The MathWorks Inc., MATLAB) is used to apply the developed PTV algorithm to the captured images [24]. Image preprocessing includes denoising and normalizing the intensity of images, which is performed for individual images. The particle detection process is performed by reducing the image to a binary array by defining a global threshold for the image. The threshold is found using Otsu's method [29], which minimizes the intraclass variance of the black and white pixels. Initially using the normalized cut-off threshold of a specific image, the particles are recognized by tracing the exterior of boundaries of objects in the binary image. A unique feature of this algorithm is that erosion is used to allow individual particles to be detected. This is an important feature when particles begin to cluster at nodes. The particle recognition algorithm is a Moore-neighbor-tracing algorithm modified by Jacob's stopping criteria [30].

The particle-tracking process is performed over the whole densification time period (1 s) using the nearest neighbor search method [31]. Image capture at 1000 fps ensures only small movement of particles between frames, allowing individual particles to be identified over the entire image series. An example of determined particle tracks is shown in Fig. 5. The locations of pressure nodes and antinodes are also shown in the figure and are determined from the densified image (i.e., Fig. 4(*b*)) of separated particles in the field of view. The trajectory of particles (and any existing bubbles) densifying to the pressure nodes and antinodes is illustrated in the figure. To compare experimental data with predicted theory, only particles that have a long time history traversing the acoustic field are used. The variation of normalized error calculated for different particle sets for different number of particles accounted is shown in Figure 12. A filtration process is also performed to remove bubbles in the field of view from the analyzed particles' trajectories based on their direction of motion. An example of such a bubble trajectory is highlighted in Fig. 5 using a rectangle.

From the acquired trajectory of particles, the velocity of each particle is available for each location in the trajectory. Due to the existence of several pressure nodes in the field of view, different particles' velocities can be mapped to a single wavelength space to allow characterization of the entire field. This is achieved via setting the reference of a velocity profile for a particle to the nearest pressure node in the field of view. Once the velocity fields for different particles are determined, the average particle velocity is determined by averaging over the individually mapped particle's velocity to a single wavelength. This average velocity can then be compared with the theoretical velocity field.

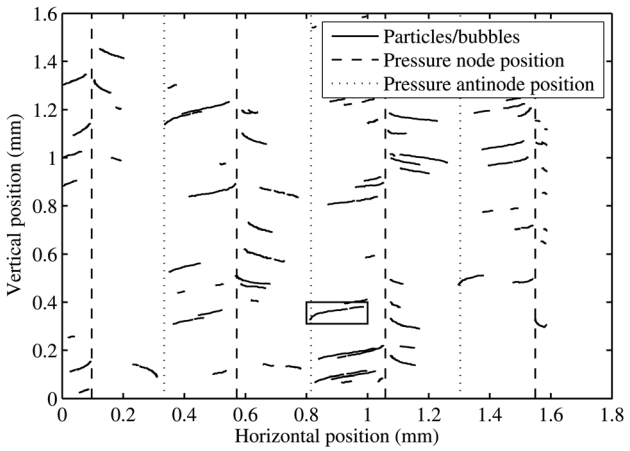

Fig. 5 Particle/bubble trajectories in the field of view in a sample pressure acoustic force experiment; while particles densify at the pressure nodes, the bubbles move to pressure antinodes. An example of a bubble motion is highlighted in the rectangle.

Uncertainty Analysis. A number of sources of uncertainties have to be considered in this study. The particle properties used in obtaining theoretical primary acoustic force are from the supplier data sheets. The particles' density and speed of sound, which are used in the calculation of ACF in Eq. (5), are with the assumption that the particle material is homogenous. This assumption is mainly challenged for PS-2 and PS-3, which are hollow glass particles and are assumed to be solid glass in acoustic contrast factor calculations. This assumption is made due to low variation of the acoustic contrast factor with respect to speed of sound for glass as shown in Fig. 1. Also, the particle size distributions and CV values, which cause a variation in the behavior of particles, are provided by the manufacturers. It is also assumed that there is no effect of secondary acoustic forces between particles present on the particles. The secondary acoustic force [32] is due to the effect of the scattered pressure field off other particles influencing the particle of interest. The magnitude of the secondary acoustic force can be compared to the primary acoustic force for dilute suspension of particles and is found to be several orders of magnitude smaller than the primary acoustic force magnitude [33]. Due to the low volume concentration (0.05%) of particles in the experiments, this force can be considered to be negligible.

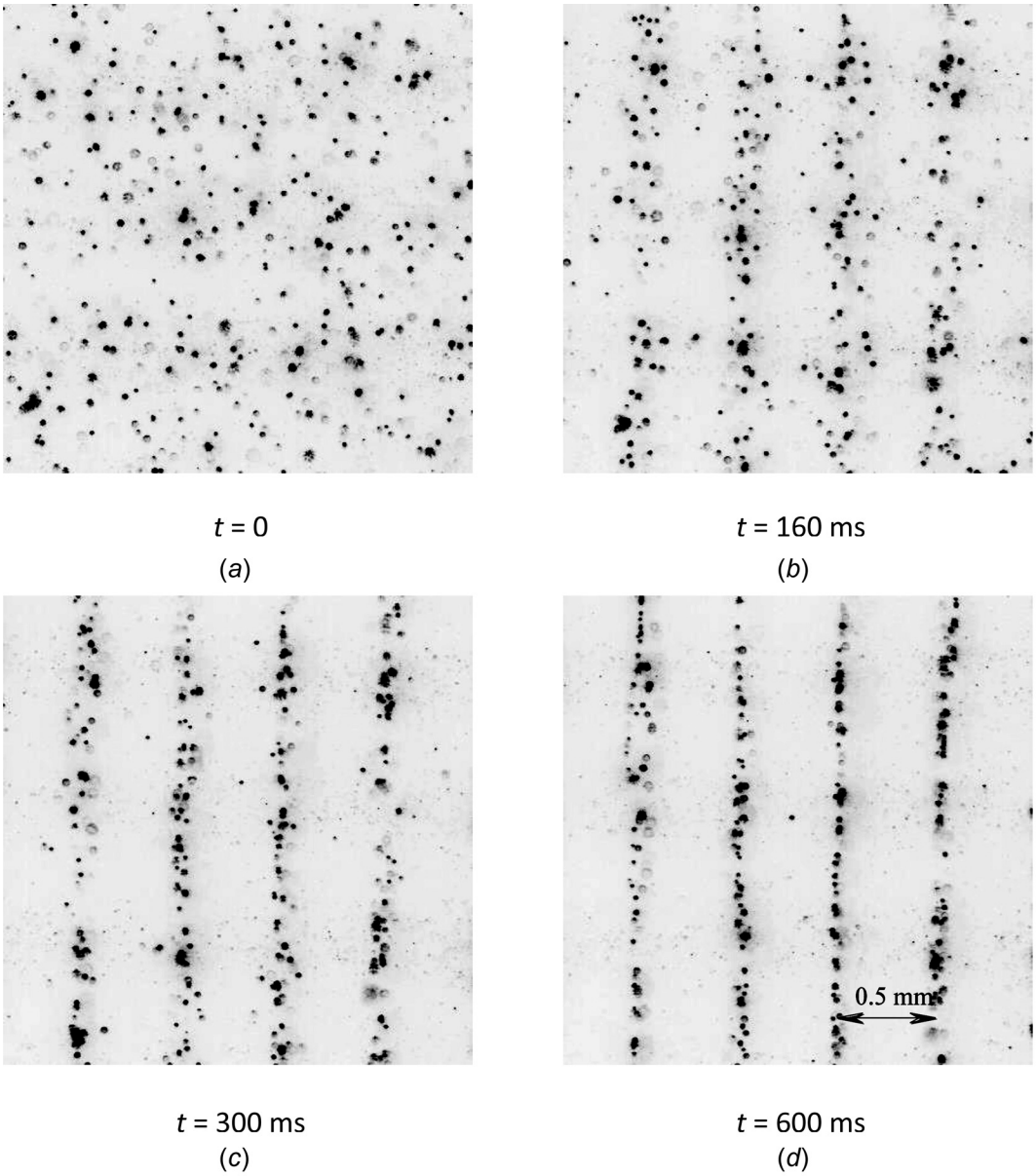

Fig. 6 Raw data images highlighting the separation process. Time increments relative to the onset of the acoustic field are shown in the figure.

Particles' locations that are obtained using the imaging system have a temporal and spatial measurement uncertainty. A temporal uncertainty of 40 ns in the triggering of the camera is the main source of the temporal uncertainty provided by the camera supplier. The maximum displacement error of 0.4 pixel is estimated as the main source of the spatial measurement uncertainty based on 0.2 pixel uncertainty in locating a particle in an image [34].

Results and Discussion

Monodispersed Particles. In order to validate the single-particle theory [23], monodispersed size distribution particles (PS-1) are first investigated. Monodispersed size distribution particles are defined as particles with particle size distribution CV lower than 10%. The resulting motion of the particles can be expected to be in lower variance, because these particles are all nearly the same size. A time series of images highlighting the gradual motion of particles to the designated pressure nodes is shown in Fig. 6. The initially randomly distributed particles are affected by the pressure acoustic force and are attracted to the closest pressure nodes based on their locations. After approximately 150 ms from the start of the experiment (triggering of the camera), the wave form to the piezoelectric transducer starts and the pressure nodes are immediately distinguishable. The separation continues until approximately 300 ms, where more particles are densified to the pressure nodes. As shown, the vertical particle bands are constant after 300 ms and there is no general motion thereafter.

Particles' locations can be normalized to a single wavelength to average their velocity located in the field of view. In order to map the particles' velocity to the normalized locations, the position of the pressure nodes where the particles densify to is needed. Image processing can be used to assess the amount of particle concentration that occurs in different regions of the field of view. In Fig. 7, a graph of image intensity summed in the vertical direction of the densified image (Fig. 6, $t = 600$ ms) is shown. The positions of pressure nodes based on particle locations are shown in the figure by dashed lines. A fast Fourier transform (FFT) is applied to this to determine the wavelength of the acoustic field, and the resultant

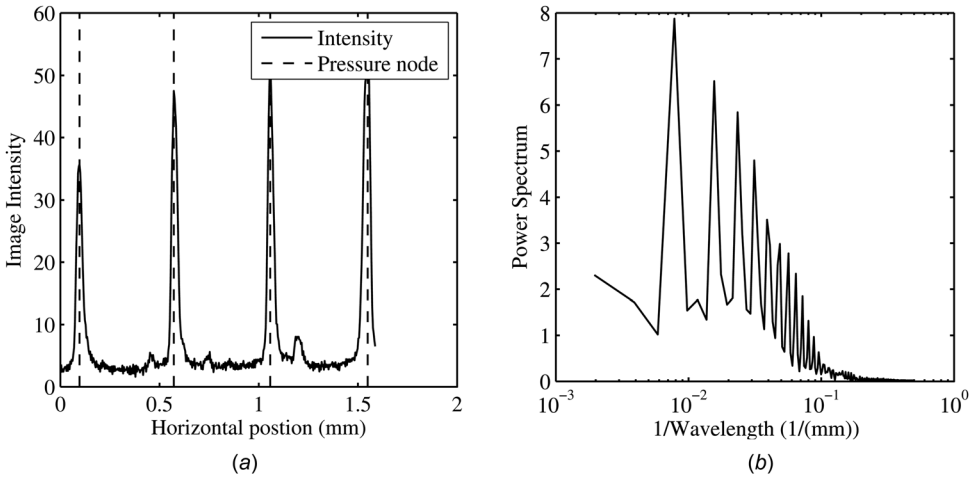

Fig. 7 (*a*) Summed intensity of Fig. 6 ($t = 600$ ms) in the x direction; locations of pressure nodes are found via these intensity plots. (*b*) FFT of the image intensity plot in Fig. 7(*a*).

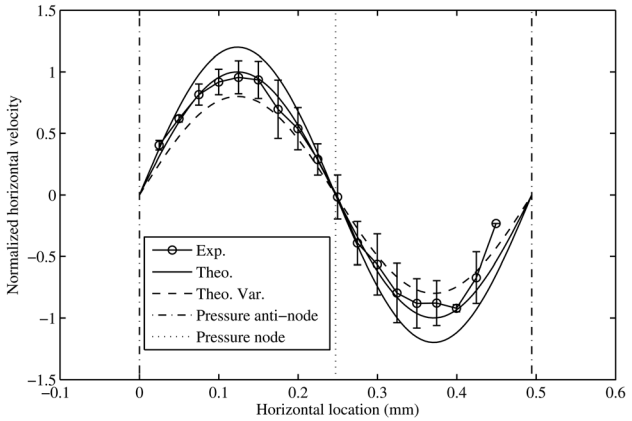

Fig. 8 Transverse velocity of PS-1, experimental versus single-particle theory values; the variation bars of experimental values fall within the theoretical variation lines shown by solid lines

power spectrum is shown in Fig. 7(*b*). The wavelength of the wave is calculated based on this graph and is 0.98 mm, which agrees with the analytical value (0.975 mm) obtained by assuming the speed of sound in water and wave frequency.

In Fig. 8, the normalized experimental measured average transverse velocity for the tracked particles over a wavelength is plotted. The particles are repelled from the two pressure antinodes at the start and end of the graph. The particles densify at the pressure node, which is the middle of the graph. Bars have been applied to the experimental data to show the range of measured velocity. The standard deviation of calculated averaged normalized velocity is used for representing the range. This range is predominantly attributed to the distribution of particle size present in the sample. The expected particle-normalized velocity determined from the single particle theory (Eq. (9)) is also plotted in the figure. Also plotted are the ranges of the theoretical variation due to an imposed particle size distribution, which show the deviation of the transverse theoretical velocity. This value (20%) is obtained based on the provided CV value of particles' size distribution, which is 10%. This figure shows that the pattern of the transverse velocity field matches the one estimated by the primary acoustic force theory for a single particle [23]. Also, the range of the measured velocity profiles (experimental standard deviation) falls within the range obtained based on the theoretical standard deviation of the size of particles.

The observed discrepancies between the experimentally measured transverse velocity and the theoretical values are larger at the pressure nodes and antinodes. At these locations, the tracking of particles is more complex, due to the overlapping of the particles, and a larger error is expected. Another issue in determining particle motion is direction change of the particles near the pressure node, which increases the variation bars of experimental transverse velocity. Observations indicate that particles can oscillate about the line of the pressure node.

Polydispersed Particles. Having determined the limits and verified the experimental method with the primary acoustic force theory for the monodispersed-sized particles, polydispersed particles (hollow glass sphere particles, PS-2, and PS-3) are investigated. The aim is to determine the validity and applicability of theoretical primary acoustic force calculation to the polydisperse particles with high CV distribution size. According to the properties of particles listed in Table 2, they will be attracted to the pressure nodes and their ACF is 0.14 and 0.35, respectively. The same experiment procedure and postprocessing algorithm are used to study the motion of particles. Sample images of densified particles are shown in Figs. 9(*a*) and 9(*b*) for the two particle groups. As it is shown, the particle densification lines are formed clearly and there are also some cavitation bubbles (negative ACF) present at the pressure antinodes. In Figs. 9(*c*) and 9(*d*), the analyzed densified images are shown. Using these intensity plots, the locations of pressure nodes are obtained and the wavelength of the wave is found to be 0.98 mm for both data sets.

In Figs. 10 and 11, the normalized experimental measured average horizontal velocities over a single wavelength for PS-2 and PS-3 are plotted, respectively. The bars located at the experimental points show the range of obtained values due to the distribution of particle size present in the sample. The theoretical horizontal velocity expected by primary acoustic force theory for a single particle is also shown in both of the figures along with the limitations of theoretical variation. These are the deviation of the horizontal theoretical velocity due to an imposed particle CV of 35% (PS-2) and 45% (PS-3) and are determined to be 64% and 88%, respectively. The experimental variation bars fall within the theoretical variation limits except for at the middle of the wavelength, where the pressure node lies. This is due to the existence of particles at both sides of the pressure node where the velocity changes direction and tracking of particles is difficult. The good agreement between the experimental and theoretical results prove that the primary acoustic force theory is applicable to polydisperse particles in the macroscale acoustic chambers for this particle

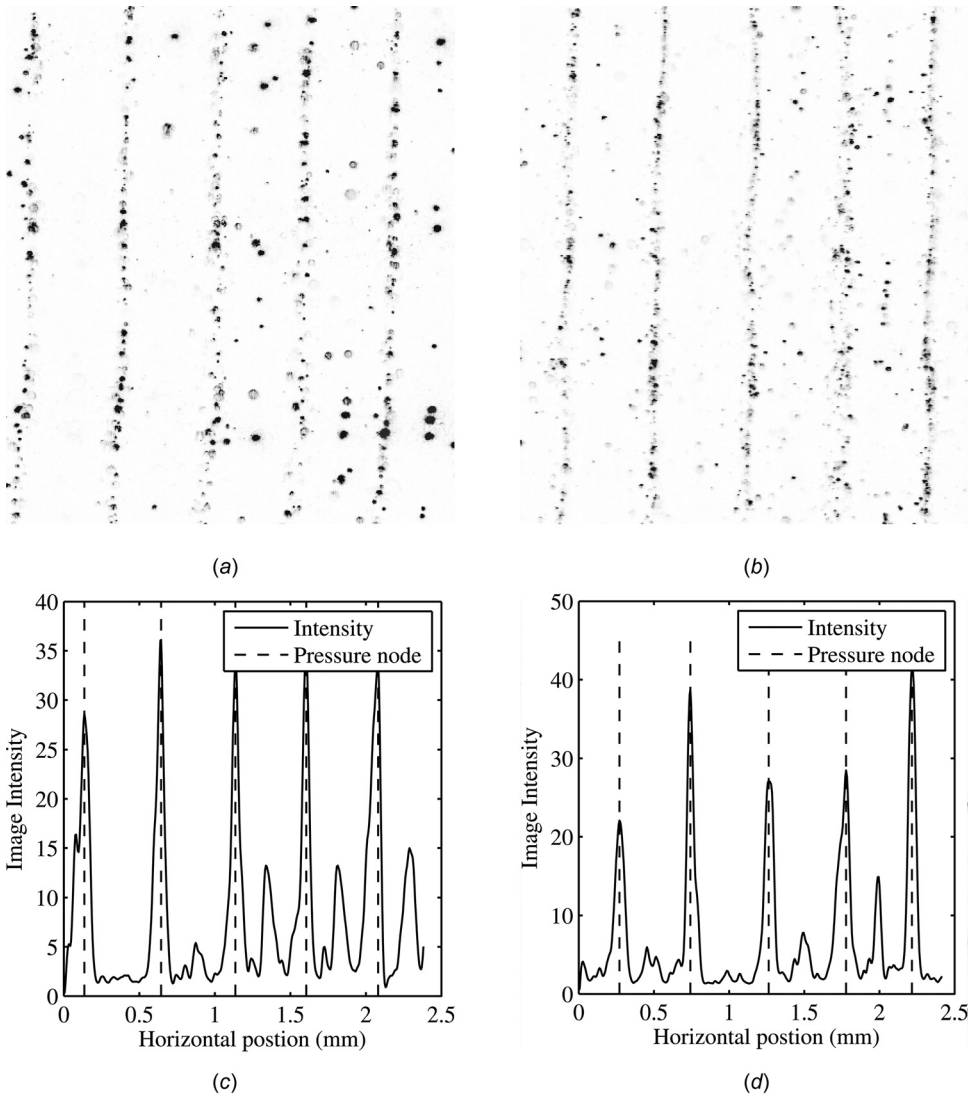

Fig. 9 (*a*) PS-2 densified image and (*b*) PS-3 densified image. (*c*) In *x* direction, locations of pressure nodes are found via these strong intensity plots for PS-2 and (*d*) intensity plot for PS-3.

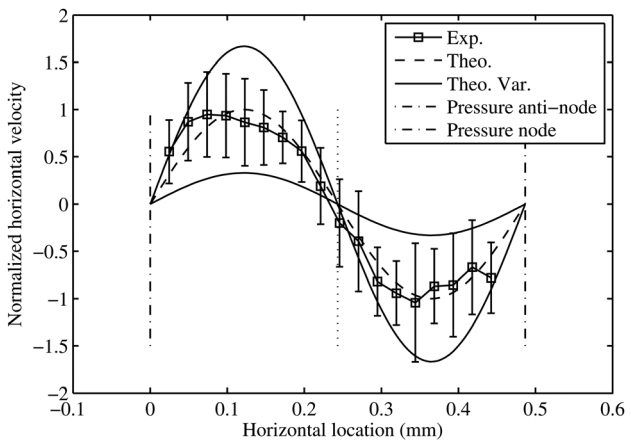

Fig. 10 Transverse velocity of PS-2: experimental versus single-particle theory values

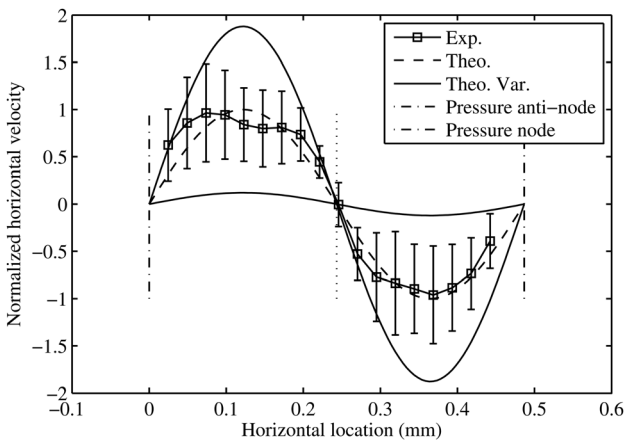

Fig. 11 Transverse velocity of PS-3: experimental versus single-particle theory values

loading. The discrepancies are mostly located near pressure nodes and antinodes. This is mostly due to overlapping of particles at the pressure nodes making them difficult to detect and also change of velocity direction at these points.

Number of Tracked Particles. To investigate the effect of the number of particles on the statistical averaging of particle velocity profiles in a single-wavelength, normalized average error is introduced. The normalized average error ($\hat{e}$) is defined to quantify the

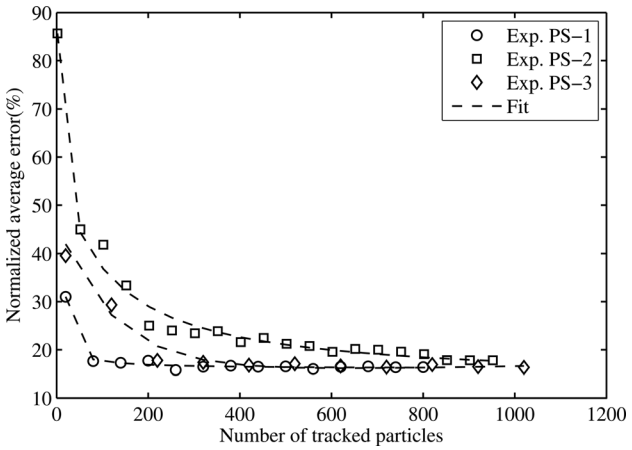

Fig. 12 Effect of number of considered particles on the normalized error in achieving horizontal velocity for PS-1, PS-2, and PS-3

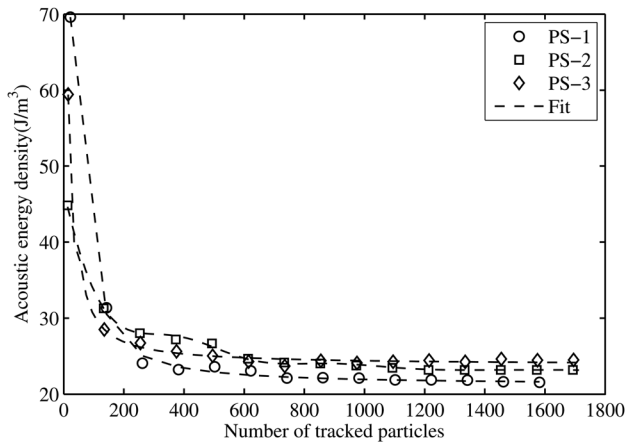

Fig. 13 Acoustic energy density independence with respect to the number of tracked particles for PS-1, PS-2, and PS-3

difference between the experimental and theoretical transverse velocity and is defined as

$$\hat{e} = \sum_{x_i=0}^{x_i=\lambda} \frac{\left|V^i_{\text{exp}} - V^i_{\text{theo}}\right|}{V^i_{\text{theo}}} \Big/ N \tag{10}$$

in which x_i is the transverse position in a single acoustic wavelength, λ is the acoustic wavelength, N is the number of points in the single wavelength, and V^i_{exp} and V^i_{theo} are the achieved experimental and theoretical velocity, respectively. This error is determined by averaging the normalized difference between the theoretical and experimental values of transverse velocity in different locations in a single acoustic wavelength (λ). The initial point and final point where the pressure antinodes lie are not counted when averaging over the wavelength of the wave, since theoretical value of velocity is zero, which results in making the normalized relative error infinity. The variation of normalized error is calculated for different particle sets for a different number of particles accounted for is shown in Fig. 12. The fitted line to the experiment data shows that there is an asymptotic trend seen in the error, and the error appears independent of the number of tracked particles for a value greater than 800. As the number of tracked particles increases, the results become independent with respect to the number of tracked particles in the analysis.

Acoustic Energy Density. The acoustic energy density is an unknown physical property of the acoustic chamber coupled to the transducer used to develop the acoustic field. Its value is affected by the coupling efficiency of acoustic energy into the chamber containing fluid and is difficult to estimate. However, based on theory, a general estimation can be determined [26]. For the system used here, it is estimated to be in the range of 10–100 J/m^3. To experimentally determine the acoustic energy density for the acoustic chamber, the maximum velocity of averaged horizontal velocity ($V_{\max}$) is used by manipulating Eq. (9) for the peak points of the average velocity profiles and is defined as

$$E_{ac} = \frac{2\pi\mu a V_{\max}}{V_0 \kappa \eta} \tag{11}$$

The evaluated acoustic energy density as a function of number of tracked particles is presented in Fig. 13. The final value of the acoustic energy density is determined when it is not varying for a different number of tracked particles, and it reaches approximately the same value for the three different experiments. The value of the acoustic energy density solely depends on acoustic chamber parameters and is expected to be the same value for different particle sets. However, due to assumptions of different particles' parameters, such as particle density and particle compressibility based on the supplier specifications, there are some variations of computed acoustic energy density for different particle sets. Taking this into account, good agreement observed between the achieved acoustic energy density for different particle sets of approximately 25 ± 2 J/m^3 is obtained. This value is within the normal range of acoustic chamber acoustic energy densities [26].

Conclusions

Applicability of the current primary acoustic force theory [23] for predicting single-particle motion in an acoustic field is investigated for macroscale, multiwavelength acoustic chambers for polydispersed particle sets. A particle-tracking velocimetry approach has been developed to track the motion of particles in water under the influence of an acoustic standing pressure wave. This particle flow field has some unique features, most notable of which is that, with time, the homogeneous distribution of particles does not remain and significant clustering of particles occurs. The PTV algorithm is optimized for this unique configuration of a separation process for monodispersed size particles and used to investigate two other different polydispersed size distribution particles. The volume concentration of particles in water for all experiments was held at 0.05%. The independence of the selected parameters in the postprocessing is presented for the three different particle size experiments. The acoustic energy density value for the acoustic chamber is also evaluated, and—as expected—the value is constant for the different particles. The results show that the primary acoustic force theory for a single particle is capable of predicting the motion of particles for polydispersed size distribution particles in macroscale, multiwavelength acoustic chambers.

Acknowledgment

This work was carried out with funding support from the Centre for Oil Sands Innovation (COSI), Alberta Ingenuity Fund, the Natural Sciences and Research Council (NSERC) of Canada, and the Canadian Foundation of Innovation (CFI).

References

[1] Grosch, M., Burger, W., Handl, B., Doblhoff-Dier, O., Gaida, T., and Schmatz, C., 1998, "Ultrasonic Separation of Suspended Particles—Part III: Application in Biotechnology,"Acustica, **84**(5), pp. 815–822.
[2] Kapishnikov, S., Kantsler, V., and Steinberg, V., 2006, "Continuous Particle Size Separation and Size Sorting Using Ultrasound in a Microchannel," J. Stat. Mech.: Theory Exp., **2006**(1), p. P01012.
[3] Ju, Y. R., Geng, Z. X., Zhang, L. Q., Wang, W., and Li, Z. H., 2011, "High-Efficiency Blood Separation Utilizing Spiral Filtration Microchannel With

Gradually Varied Width," Solid-State Sensors, Actuators and Microsystems Conference (TRANSDUCERS), pp. 298–301.
[4] Dayton, P. A., Zhao, S., Bloch, S. H., Schumann, P., Penrose, K., Matsunaga, T. O., Zutshi, R., Doinikov, A., and Ferrara, K. W., 2006, "Application of Ultrasound to Selectively Localize Nanodroplets for Targeted Imaging and Therapy," Mol. Imaging, **5**(3), pp. 160–174.
[5] Lum, A. F. H., Borden, M. A., Dayton, P. A., Kruse, D. E., Simon, S. I., and Ferrara, K. W., 2006, "Ultrasound Radiation Force Enables Targeted Deposition of Model Drug Carriers Loaded on Microbubbles," J. Control. Release, **111**(1–2), pp. 128–134.
[6] Weller, G. E. R., Villanueva, F. S., Tom, E. M., and Wagner, W. R., 2005, "Targeted Ultrasound Contrast Agents: In Vitro Assessment of Endothelial Dysfunction and Multi-targeting to ICAM-1 and Sialyl Lewisx," Biotechnol. Bioeng., **92**(6), pp. 780–788.
[7] King, L. V., 1934, "On the Acoustic Radiation Pressure on Spheres," Proc. R. Soc. Lond. A, **147**(861), pp. 212–240.
[8] Settnes, M., and Bruus, H., 2012, "Forces Acting on a Small Particle in an Acoustical Field in a Viscous Fluid," Phys. Rev. E, **85**(1), p. 016327.
[9] Yosioka, K., and Kawasima, Y., 1955, "Acoustic Radiation Pressure on a Compressible Sphere," Acustica, **5**(3), pp. 167–173.
[10] Nilsson, A., Petersson, F., Jönsson, H., and Laurell, T., 2004, "Acoustic Control of Suspended Particles in Micro Fluidic Chips," Lab Chip, **4**(2), pp. 131–135.
[11] Petersson, F., Nilsson, A., Holm, C., Jonsson, H., and Laurell, T., 2004, "Separation of Lipids From Blood Utilizing Ultrasonic Standing Waves in Microfluidic Channels," Analyst, **129**(10), pp. 938–943.
[12] Glynne-Jones, P., Boltryk, R. J., Hill, M., Harris, N. R., and Baclet, P., 2009, "Robust Acoustic Particle Manipulation: A Thin-Reflector Design for Moving Particles to a Surface," J. Acoust. Soc. Am., **126**(3), pp. EL75–EE79.
[13] Ho, L., Braun, K., Fabris, R., Hoefel, D., Morran, J., Monis, P., and Drikas, M., 2012, "Comparison of Drinking Water Treatment Process Streams for Optimal Bacteriological Water Quality," Water Res., **46**(12), pp. 3934–3942.
[14] Hafez, A., Khedr, M., and Gadallah, H., 2007, "Wastewater Treatment and Water Reuse of Food Processing Industries. Part II: Techno-Economic Study of a Membrane Separation Technique," Desalination, **214**(1–3), pp. 261–272.
[15] Juliano, P., Kutter, A., Cheng, L. J., Swiergon, P., Mawson, R., and Augustin, M. A., 2011, "Enhanced Creaming of Milk Fat Globules in Milk Emulsions by the Application of Ultrasound and Detection by Means of Optical Methods," Ultrason. Sonochem., **18**(5), pp. 963–973.
[16] Lipkens, B., Dionne, J., Trask, A., Szczur, B., Stevens, A., and Rietman, E., 2010, "Separation of Micron-Sized Particles in Macro-scale Cavities by Ultrasonic Standing Waves," Phys. Procedia, **3**(1), pp. 263–268.
[17] Hawkes, J. J., and Radel, S., 2013, "Acoustofluidics 22: Multi-wavelength Resonators, Applications and Considerations," Lab Chip, **13**(4), pp. 610–627.
[18] Bruus, H., 2012, "Acoustofluidics 10: Scaling Laws in Acoustophoresis," Lab Chip, **12**(9), pp. 1578–1586.
[19] Spengler, J. F., Jekel, M., Christensen, K. T., Adrian, R. J., Hawkes, J. J., and Coakley, W. T., 2001, "Observation of Yeast Cell Movement and Aggregation in a Small-Scale MHz-Ultrasonic Standing Wave Field," Bioseparation, **9**(6), pp. 329–341.
[20] Woodside, S. M., Bowen, B. D., and Piret, J. M., 1997, "Measurement of Ultrasonic Forces for Particle–Liquid Separations," AIChE J., **43**(7), pp. 1727–1736.
[21] Barnkob, R., Augustsson, P., Laurell, T., and Bruus, H., 2010, "Measuring the Local Pressure Amplitude in Microchannel Acoustophoresis," Lab Chip, **10**(5), pp. 563–570.
[22] Augustsson, P., Barnkob, R., Wereley, S. T., Bruus, H., and Laurell, T., 2011, "Automated and Temperature-Controlled Micro-PIV Measurements Enabling Long-Term-Stable Microchannel Acoustophoresis Characterization," Lab Chip, **11**(24), pp. 4152–4164.
[23] Gorkov, L. P., 1962, "On the Forces Acting on a Small Particle in an Acoustic Field in an Ideal Fluid," Sov. Phys. Doklady, **6**, pp. 773–775.
[24] Setayeshgar, A., Lipsett, M. G., Koch, C. R., and Nobes, D. S., 2013, "Measurement of Particle Dynamics in a Coherent Acoustic Field," 10th International Symposium on Particle Image Velocimetry.
[25] Kundt, A., and Lehmann, O., 1874, "Longitudinal Vibrations and Acoustic Figures in Cylindrical Columns of Liquids," Ann. Phys. Chem., **153**, pp. 1–11.
[26] Bruus, H., 2012, "Acoustofluidics 7: The Acoustic Radiation Force on Small Particles," Lab Chip, **12**(6), pp. 1014–1021.
[27] Trampler, F., Sonderhoff, S. A., Pui, P. W. S., Kilburn, D. G., and Piret, J. M., 1994, "Acoustic Cell Filter for High Density Perfusion Culture of Hybridoma Cells," Nat. Biotech., **12**(3), pp. 281–284.
[28] Hawkes, J. J., Coakley, W. T., Groschl, M., Benes, E., Armstrong, S., Tasker, P. J., and Nowotny, H., 2002, "Single Half-Wavelength Ultrasonic Particle Filter: Predictions of the Transfer Matrix Multilayer Resonator Model and Experimental Filtration Results," J. Acoust. Soc. Am., **111**(3), pp. 1259–1266.
[29] Otsu, N., 1979, "A Threshold Selection Method From Gray-Level Histograms," IEEE Trans. Syst., Man, and Cybernetics, **9**(1), pp. 62–66.
[30] Pavlidis, T., 1982, *Algorithms for Graphics and Image Processing*, Computer Science, Rockville, MD.
[31] Hassan, Y. A., and Canaan, R. E., 1991, "Full-Field Bubbly Flow Velocity Measurements Using a Multiframe Particle Tracking Technique," Exp. Fluids, **12**(1–2), pp. 49–60.
[32] Doinikov, A. A., 2001, "Acoustic Radiation Interparticle Forces in a Compressible Fluid," J. Fluid Mech., **444**(1), pp. 1–21.
[33] Hancock, A., 2001, "*Observation of Forces on Microparticles in Acoustic Standing Waves*," M.Sc. thesis, University of California Davis, Davis, CA.
[34] Feng, Y., Goree, J., and Liu, B., 2007, "Accurate Particle Position Measurement From Images," Rev. Sci. Instrum., **78**(5), p. 053704.